

SENSIBLE HEAT EXCHANGE AT THE ANTARCTIC SNOW SURFACE: A STUDY WITH AUTOMATIC WEATHER STATIONS

MICHEL VAN DEN BROEKE,* DIRK VAN AS, CARLEEN REIJMER and RODERIK VAN DE WAL
Institute for Marine and Atmospheric Research, Utrecht University, PO Box 80005, 3508 TA Utrecht, The Netherlands

Received 8 April 2004

Revised 22 November 2004

Accepted 22 November 2004

ABSTRACT

Data of four automatic weather stations (AWSs) are used to calculate the turbulent exchange of sensible heat at the Antarctic snow surface for a 4 year period (1998–2001). The AWSs are situated on the ice shelf, in the coastal/inland katabatic wind zone and on the interior plateau in Dronning Maud Land, East Antarctica. Sensible heat flux (SHF) is calculated using the aerodynamic ‘bulk’ method between a single AWS sensor level and the surface, in combination with surface temperature derived from upwelling longwave radiation and surface roughness derived from eddy correlation measurements. Good agreement is found between calculated and directly measured SHF. All AWS sites show a downward-directed average sensible heat transport, but otherwise the differences between the various zones are large. The surface roughness for momentum differs by an order of magnitude between the interior plateau (0.02 mm) and the katabatic wind zone (0.16 mm). On the ice shelf, frequent clouds limit surface cooling, and annual mean SHF is small (8 W m^{-2}). In contrast, clear skies prevail on the interior plateau, but weak winds, an aerodynamically smooth surface and stability effects limit annual mean SHF to an equally low value (8 W m^{-2}). The most favourable conditions for sensible heat exchange are found in the katabatic wind zone, where a combination of strong winds, relatively little cloud cover and a rougher surface results in annual mean SHF values of 22 to 24 W m^{-2} . Copyright © 2005 Royal Meteorological Society.

KEY WORDS: heat exchange; snow surface; Antarctica; energy balance

1. INTRODUCTION

To assess the role of the Antarctic ice sheet as a major heat sink in the climate system, the exchange of sensible heat at its snow surface must be quantified. The proper framework for this is the surface energy balance (SEB):

$$\begin{aligned} M &= \text{SHW} \downarrow + \text{SHW} \uparrow + \text{LW} \downarrow + \text{LW} \uparrow + \text{SHF} + \text{LHF} + G \\ &= R_{\text{net}} + \text{SHF} + \text{LHF} + G \end{aligned} \quad (1)$$

where M is melting energy ($M = 0$ if the surface temperature $T_s < 273.15 \text{ K}$), $\text{SHW} \downarrow$ and $\text{SHW} \uparrow$ are incoming and reflected shortwave radiation fluxes, $\text{LW} \downarrow$ and $\text{LW} \uparrow$ are incoming and emitted longwave radiation fluxes, SHF and LHF are the turbulent fluxes of sensible and latent heat and G is the subsurface conductive heat flux. All terms are evaluated at the surface and are defined positive when directed towards the surface.

Averaged over the globe and year, SHF is negative on average, but it constitutes a considerably smaller surface heat sink than does evaporation (LHF). Over the ice sheet of Antarctica, the situation is very different: the snow surface is highly reflective for shortwave radiation, while it effectively loses heat in the form of

*Correspondence to: Michiel van den Broeke, Institute for Marine and Atmospheric Research Utrecht, Utrecht University, PO Box 80005, 3508 TA Utrecht, The Netherlands; e-mail: broeke@phys.uu.nl

longwave radiation to the cold and clear overlying atmosphere. As a result, the surface is generally colder than the air, making SHF positive. At the same time, LHF is generally small, because low temperatures limit the absolute moisture content and therewith surface-to-air moisture gradients. Over the coastal slope of the ice sheet, cooling of the near-surface air forces strong and persistent katabatic winds. These winds provide the shear necessary to maintain turbulent exchange in the stably stratified surface layer (SL), especially in winter.

Quantifying SHF at the Antarctic snow surface requires eddy correlation measurements. Most Antarctic meteorological experiments dedicated to quantify SEB components have been summer-only type (Wendler *et al.*, 1988; Heinemann and Rose, 1990; Bintanja and van den Broeke, 1995; Bintanja, 2000; van As *et al.*, 2005a). Only a few experiments have covered the entire annual cycle (Liljequist, 1957; Carroll, 1982; Ohata *et al.*, 1985; King *et al.*, 1996), and these were often undertaken close to manned stations for reasons of power supply and sensor maintenance. Unfortunately, the network of manned meteorological stations in Antarctica is sparse and heavily biased towards the coast, where climate conditions are very different from the high interior plateau and the katabatic wind zone in between.

Using automatic weather stations (AWSs) can remedy part of the problem of poor data coverage in Antarctica. In recent decades, AWSs have been used successfully to monitor basic climate variables such as atmospheric pressure, temperature and wind in inland Antarctica (Allison *et al.*, 1993; Renfrew and Anderson, 2002). When AWSs are equipped with sonic height rangiers, precipitation events can be monitored (Reijmer and van den Broeke, 2003) to support the interpretation of climate records in firn/ice cores (Helsen *et al.*, in press). If humidity measurements are available, then similarity theory may be used to calculate sublimation from AWS data (Clow *et al.*, 1988; Stearns and Weidner, 1993; van den Broeke *et al.*, in press a). Reliable radiation sensors deployed on AWSs have improved our knowledge of the surface radiation balance in Antarctica (van den Broeke *et al.*, 2004a,b). In combination with a subsurface snow model, the full annual cycle of the SEB may be calculated from AWS data (Bintanja *et al.*, 1997; Reijmer and Oerlemans, 2002; van den Broeke *et al.*, in press b).

In this paper we focus on the exchange of sensible heat (SHF) using observations of four AWSs in Dronning Maud Land (DML), East Antarctica. In Section 2 we present the AWS sensor specifications, data treatment and methods to calculate the SHF from single-level AWS data. Results are presented in Section 3, a discussion in Section 4 and a summary in Section 5.

2. METHODS

2.1. AWS description and sensor specifications

The AWSs are situated along a traverse line in DML, East Antarctica (Figure 1). AWS 4 is a coastal station, located on the Riiser-Larsen ice shelf some 80 km away from the ice shelf front and 40 km from the ice sheet grounding line. AWS 5 is located just inland of the grounding line, on the steep coastal slopes of the ice sheet. AWS 6 is situated at the foot of the Heimefront Mountains in the katabatic wind zone, also in a region with a relatively large surface slope. AWS 9 is situated on Amundsenisen on the interior plateau, where the surface is relatively flat. In a radius of at least several kilometres, the surroundings of the AWSs consist of an undisturbed snow surface.

All four AWSs are similar in design; a picture of AWS 9 is shown in Figure 2 and sensor specifications are given in Table I. Single-level measurements of wind, temperature T and relative humidity RH are performed at a height of approximately 3 m at the date of installation. The RH measurements have been corrected according to the method proposed by Anderson (1994). The individual radiation components (SHW \downarrow , SHW \uparrow , LW \downarrow , LW \uparrow) are measured with a single sensor. Air pressure is measured in the electronics enclosure, which is buried in the snow. Snow temperatures are measured at initial depths of 0.05, 0.1, 0.2, 0.4, 0.8, 2, 4, 6, 10 and 15 m. This depth, as well as the height of the AWS instruments, changes continuously as snow accumulates/ablates from the surface, and is monitored with a sonic height ranger. The sampling interval for pressure is 30 min (instantaneous value); all other sensors are sampled at 6 min intervals (instantaneous, except for wind speed, cumulative) after which 2 h averages are stored in a Campbell CR10 datalogger.

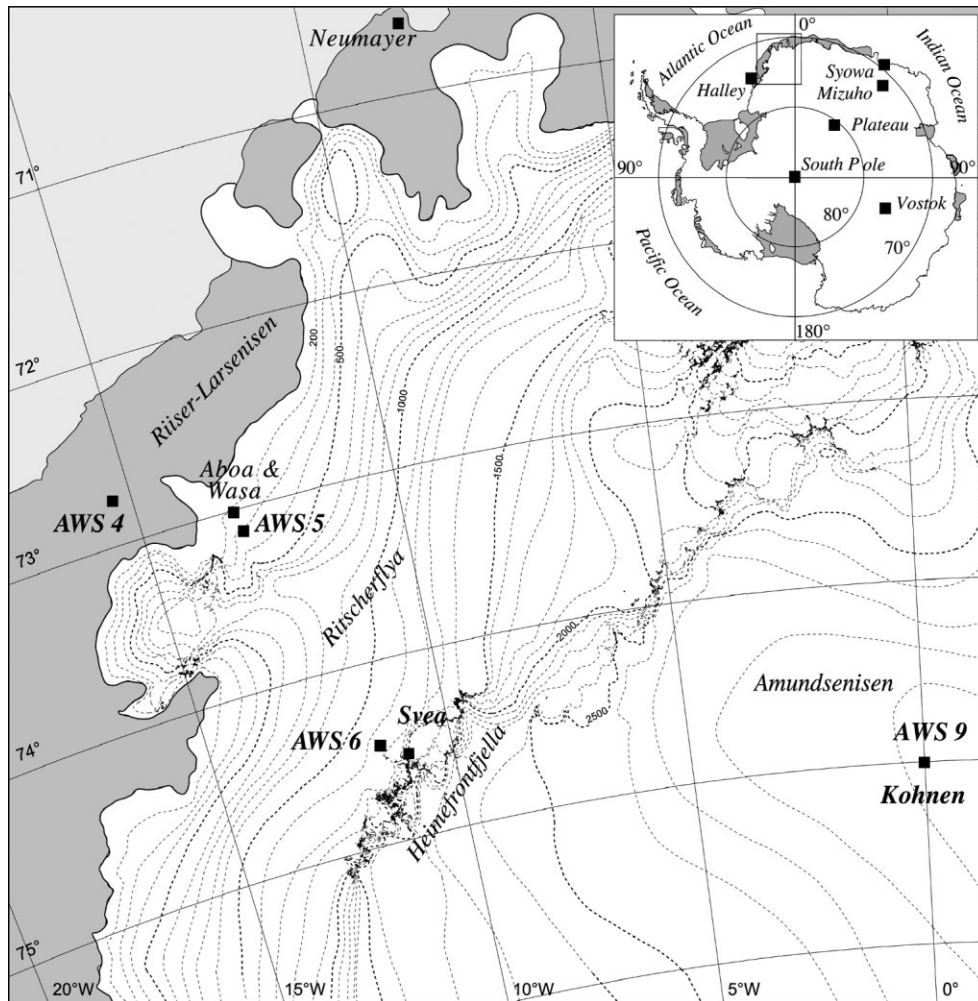


Figure 1. Map of western DML, Antarctica, with AWS locations, main topographical features, ice shelves (grey), height contours (dashed lines, every 100 m) and scientific station locations

Energy considerations do not allow aspiration of the temperature/humidity sensors. On-site comparisons with ventilated instruments show that radiation errors in temperature readings do not exceed the uncertainty arising from instrument accuracy. For instance, a 24 day comparison near AWS 6 in January and February 1998 revealed a mean difference of only 0.01 K in the 2 h averages with a root-mean-squared difference (RMSD) of 0.22 K. Basic topographical and climate information of the AWS sites is given in the upper part of Table II.

2.2. Calculation of the SHF from single-level AWS data

The surface turbulent SHF is calculated using

$$\text{SHF} = -\rho c_p \overline{(w'\theta')}_s = \rho c_p u_* \theta_* \quad (2)$$

in which ρ is air density, c_p the heat capacity of dry air at constant pressure (assumed constant $c_p = 1005 \text{ J kg}^{-1} \text{ K}^{-1}$), w' and θ' are the turbulent fluctuations of vertical velocity and potential temperature and u_* and θ_* are the associated turbulent scales. Having only one AWS measurement level at our disposal, the

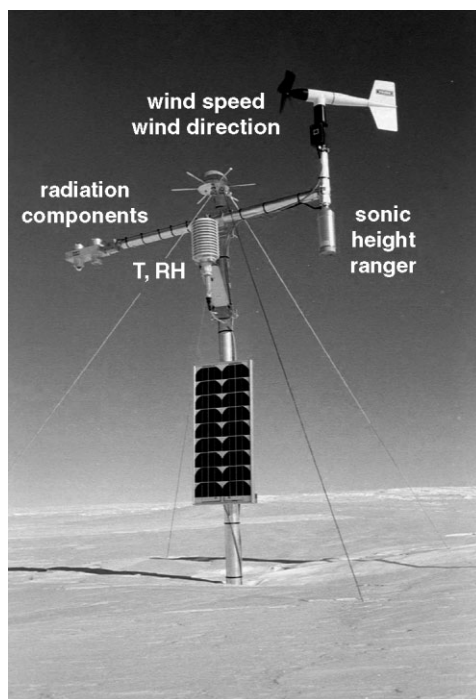


Figure 2. Picture of AWS 9. The datalogger and pressure sensor are buried in the snow. The other AWSs have similar designs

Table I. AWS sensor specifications

Sensor	Type	Range	Accuracy ^a
Air pressure	Vaisala PTB101B	600 to 1060 hPa	4 hPa
Air temperature	Vaisala HMP35AC	-80 to +56 °C	0.3 °C
Relative humidity	Vaisala HMP35AC	0 to 100%	2% (RH < 90%) 3% (RH > 90%)
Wind speed	Young 05 103	0 to 60 m s ⁻¹	0.3 m s ⁻¹
Wind direction	Young 05 103	0 to 360°	3°
Pyranometer	Kipp en Zonen CM3	305 to 2800 nm	EADT ±10%
Pyrradiometer	Kipp en Zonen CG3	5000 to 50 000 nm	EADT ±10%
Snow height	Campbell SR50	0.5 to 10 m	0.01 m or 0.4%

^a EADT: estimated accuracy of daily total.

turbulent scales are calculated using the 'bulk' method, a robust method that relates turbulence scales to differences in wind speed V , potential temperature θ and specific humidity q between a single measurement level and the snow surface:

$$\begin{aligned}
 u_* &\cong \frac{\kappa[V(z_V) - V(z_{0,V})]}{\ln\left(\frac{z_V}{z_{0,V}}\right) - \Psi_m\left(\frac{z_V}{L_{MO}}\right) + \Psi_m\left(\frac{z_{0,V}}{L_{MO}}\right)} \\
 \theta_* &\cong \frac{\kappa[\theta(z_T) - \theta(z_{0,T})]}{\ln\left(\frac{z_T}{z_{0,T}}\right) - \Psi_h\left(\frac{z_T}{L_{MO}}\right) + \Psi_h\left(\frac{z_{0,T}}{L_{MO}}\right)}
 \end{aligned}
 \tag{3}$$

Table II. AWS topographic and climate characteristics, 1998–2001. RH is given with respect to ice. For temperature, RH and specific humidity, the mean value at AWS sensor level (approximately 2 m) is given. Wind speed is extrapolated from AWS sensor level (approximately 3 m) to 10 m using flux-profile relations

	AWS 4	AWS 5	AWS 6	AWS 9
<i>Location</i>				
Latitude	72°45.2'S	73°06.3'S	74°28.9'S	75°00.2'S
Longitude	15°29.9'W	13°09.9'W	11°31.0'W	0°00.4'E
Elevation (m a.s.l.)	34	363	1160	2892
Surface slope (m km ⁻¹)	<1	13.5	15	1.3
<i>Period of observation used for this paper</i>				
Start of observation	22 Dec 1997	3 Feb 1998	14 Jan 1998	1 Jan 1998
End of observation	21 Dec 2001	2 Feb 2002	13 Jan 2002	31 Dec 2001
<i>Basic climate variables, annual mean</i>				
Pressure (hPa)	979	941	854	673
Temperature (K)	254.3	256.8	252.6	230.0
Air density (kg m ⁻³)	1.34	1.28	1.18	1.02
RH (%)	93	83	78	93
Specific humidity (g kg ⁻¹)	1.03	1.01	0.72	0.17
10 m wind speed (m s ⁻¹)	5.7	7.8	7.7	4.8
Surface albedo	0.88	0.84	0.84	0.85
R_{net} (W m ⁻²)	-7.0	-15.6	-22.1	-6.9
<i>Sensible heat variables, annual mean</i>				
SHF (W m ⁻²)	7.6	21.7	24.1	8.0
KHF (10 ⁻³ K m s ⁻¹)	5.6	16.9	20.3	7.8
$z_{0,V}$ (mm)	0.1	0.16	0.16	0.02
$z_{0,T}/z_{0,V}$	1.42	0.59	0.61	3.44
θ_* (K)	0.040	0.067	0.084	0.068
u_* (m s ⁻¹)	0.193	0.277	0.268	0.137
KHF/ $u_*\theta_*$	0.73	0.91	0.90	0.84
SHF($\Psi_m = \Psi_h = 0$) (W m ⁻²)	9.3 (+22%)	24.3 (+12%)	27.7 (+15%)	10.6 (+33%)

in which L_{MO} is a length scale following from Monin–Obukhov similarity theory:

$$L_{\text{MO}} = \frac{u_*^2}{\kappa \frac{q}{\theta} (\theta_* + 0.62\theta q_*)} \quad (4)$$

which in turn requires knowledge of the turbulent moisture scale q_* :

$$q_* \cong \frac{\kappa [q(z_q) - q(z_{0,q})]}{\ln\left(\frac{z_q}{z_{0,q}}\right) - \Psi_h\left(\frac{z_q}{L_{\text{MO}}}\right) + \Psi_h\left(\frac{z_{0,q}}{L_{\text{MO}}}\right)} \quad (5)$$

κ is the von Kármán constant ($\kappa = 0.4$), and V , θ and q are wind speed, potential temperature and specific humidity measured at AWS sensor heights z_V , z_T and z_q respectively. The RH and T sensors are in the same housing, so that $z_q = z_T$, whereas z_V is greater by about 0.75 m (Figure 2). z_V , z_q and z_T change due to accumulation/ablation at the snow surface and are continuously tracked using a sonic height ranger. Ψ_m and Ψ_h are the vertically integrated stability correction functions for momentum and heat respectively. For stable conditions ($z/L_{\text{MO}} \geq 0$) we use functions proposed by Holtslag and de Bruijn (1988), which behave most consistently in the very stable limit where turbulence ceases (Andreas, 2002). For unstable conditions ($z/L_{\text{MO}} < 0$) the functions of Dyer (1974) are used. Because L_{MO} depends on the turbulent scales, Equations (3), (4) and (5) are solved iteratively.

The surface ‘roughness’ lengths for momentum ($z_{0,V}$), specific humidity ($z_{0,q}$) and temperature ($z_{0,T}$) are defined as the levels where V , q and θ extrapolate towards their surface values. Based on a surface renewal model, in which eddies continuously scour the surface, exchanging heat and moisture, Andreas (1987) relates $z_{0,q}$ and $z_{0,T}$ to $z_{0,V}$ through the roughness Reynolds number $Re_* = u_* z_0 \nu^{-1}$:

$$\begin{aligned} \ln\left(\frac{z_{0,T}}{z_{0,V}}\right) &= c_1 - c_2 \ln(Re_*) - c_3 [\ln(Re_*)]^2 \\ \ln\left(\frac{z_{0,q}}{z_{0,V}}\right) &= c_4 - c_5 \ln(Re_*) - c_6 [\ln(Re_*)]^2 \end{aligned} \quad (6)$$

where ν is the kinematic viscosity of air (a function of air density) and c_1 to c_6 are constants given in Andreas (1987). Equation (6) is valid for rough flow ($Re_* > 2.5$); below this value a linear transition towards smooth flow is prescribed ($Re_* < 0.135$), for which $z_{0,q}/z_{0,V}$ and $z_{0,T}/z_{0,V}$ are assumed constant. Note that, over snow, typically $z_{0,V} \ll z_V$, $z_{0,q} \ll z_q$ and $z_{0,T} \ll z_T$, so that the third terms in the denominators of Equations (3) and (5) represent a very small correction. Andreas (2002) presents some experimental evidence for the validity of Equation (6), although a real validation over snow is not yet available.

The effects of drifting snow are not taken into account in the calculation of SHF. Drifting snow increases u_* , because suspended snow particles continuously extract energy from the flow (Wamser and Lykossov, 1995; Mann *et al.*, 2000; Bintanja, 2001). When drifting snow particles sublime, they extract heat and add moisture to the SL (Déry *et al.*, 1998). The resulting error in the calculated SHF is believed to be small, because the high wind speeds necessary for significant snowdrift are often associated with overcast conditions, a near-neutral SL and small values of SHF.

By definition $V(z_{0,V}) = 0$. We assume the snow surface to be saturated with respect to ice, i.e. $q(z_{0,q})$ is known when surface temperature $T_s = T(z_{0,T})$ is known. This leaves as unknowns the surface ‘roughness’ length for momentum $z_{0,V}$ and surface temperature T_s (next sections).

2.3. Determination of the surface roughness length for momentum

Equation (3) is used to express $z_{0,V}$ as a function of wind speed and friction velocity, where the Ψ_m term involving $z_{0,V}$ has been neglected:

$$\frac{V(z_V)\kappa}{u_*} \cong \ln\left(\frac{z_V}{z_{0,V}}\right) - \Psi_m\left(\frac{z_V}{L_{MO}}\right) \quad (7)$$

We used eddy-correlation measurements of u_* collected near AWS 6 in January–February 1998 (Bintanja, 2000) and near AWS 9 in January–February 2002 (van As *et al.*, 2005a). To reduce scatter and to be consistent with AWS measurements, we calculated 2 h means of $V(z_V)$ and u_* . In order not to depend on the choice of Ψ_m we selected data for which the second term on the right can be neglected, requiring it to be an order of magnitude smaller than the first term (near-neutral conditions). For $z_{0,V} = 0.1$ and 1 mm (a typical range for Antarctic snow) and $z_V = 2$ m this meant rejecting all data where $z_V/L_{MO} > 0.2$ and $z_V/L_{MO} > 0.15$ respectively. To be on the safe side, we only used data with $z_V/L_{MO} < 0.1$. To exclude snowdrift episodes, we also rejected measurements with $u_* > 0.3$ m s⁻¹. This is a typical threshold friction velocity for snowdrift (Déry and Yau, 2002), although a wide range of threshold friction velocities has been reported for various types of snow (Li and Pomeroy, 1997; Gallée *et al.*, 2001).

Linear fits made to the selected data (Figure 3) yield values for $z_{0,V}$ of 0.16 mm at AWS 6 and 0.021 mm at AWS 9. These values are well within the range of $z_{0,V}$ values reported for Antarctic snow (King and Turner, 1997), but it is surprising to find an order of magnitude difference over seemingly similar snow surfaces. A possible explanation is that small sastrugi and stronger (summer) sublimation in the katabatic wind zone (AWS 6) create a rougher surface. No eddy correlation data are available for the sites of AWSs 4 and 5. For AWS 5, which has a similar climate to AWS 6, we use $z_{0,V} = 0.16$ mm; for AWS 4 we use $z_{0,V} = 0.1$ mm, in line with values reported from nearby ice-shelf stations Halley and Neumayer (Heinemann, 1988; King and Anderson, 1994). At present we have no information about the temporal variation of $z_{0,V}$ and assume it

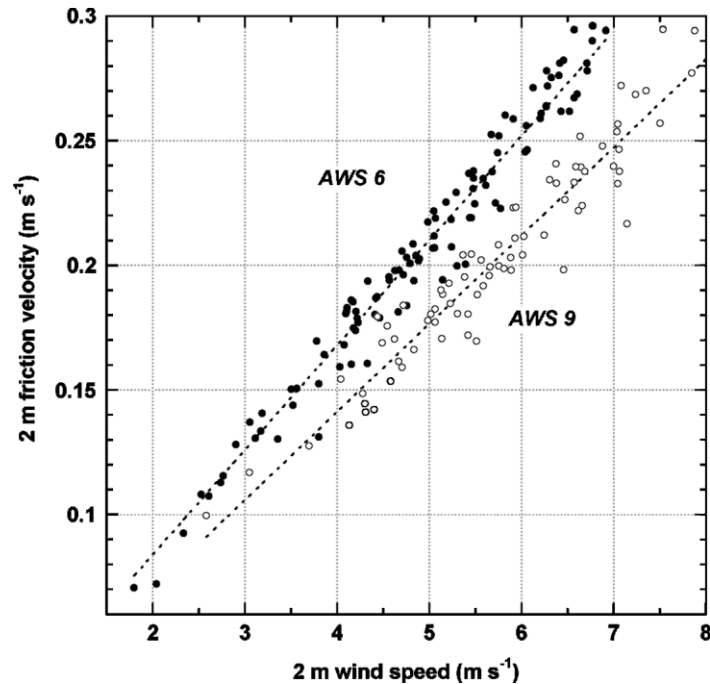


Figure 3. Determination of surface roughness for momentum $z_{0,v}$ at AWS 6 (black dots) and AWS 9 (white dots), using 2 h mean friction velocity and wind speed from eddy correlation measurements. For data selection criteria, see text

to be constant in time. Future work will include year-round eddy-correlation measurements at the AWS sites to monitor the evolution of $z_{0,v}$ in time.

2.4. Determination of surface temperature

The surface temperature T_s is solved using

$$\begin{aligned}\sigma T_s^4 &= \frac{\varepsilon - 1}{\varepsilon} LW \downarrow - \frac{1}{\varepsilon} LW \uparrow \\ &= -LW \uparrow + \frac{\varepsilon - 1}{\varepsilon} LW_{\text{net}}\end{aligned}\quad (8)$$

where $\sigma = 5.67 \times 10^{-8} \text{ W m}^{-2} \text{ K}^{-4}$ is the Stefan–Boltzmann constant, ε the surface longwave emissivity (unknown) and $LW_{\text{net}} = LW \uparrow + LW \downarrow$. Because sign and magnitude of SHF are determined by the relatively small temperature difference between the surface and the AWS sensor, it is vital that T_s is determined with sufficient accuracy. The influence of instrumental errors and the choice of ε on the calculated T_s are discussed below.

The radiation sensors used on the AWS are of secondary standard (Table I) and are, furthermore, unventilated and unheated. To assess the accuracy of the $LW \uparrow$ measurement we compared an AWS-type radiation sensor with measurements from Neumayer for an 8 day period in February 2002 (van den Broeke *et al.*, 2004b). Neumayer is a station of the Baseline Surface Radiation Network (BSRN; Ohmura *et al.*, 1998) where radiation sensors of a high standard are ventilated and checked daily. The comparison (Figure 4) shows very good agreement with an average error $<1 \text{ W m}^{-2}$ and a RMSD $<3 \text{ W m}^{-2}$, corresponding to $<0.7^\circ\text{C}$ uncertainty in T_s . The good performance of the AWS $LW \uparrow$ sensor has been confirmed for the polar plateau by extrapolating shallow snow temperatures to the surface (van As *et al.*, 2005b).

In this study we assume $\varepsilon = 1$, but Wiscombe and Warren (1980) state that ε may be as low as 0.98. The impact of this uncertainty on calculated T_s depends on LW_{net} (Equation (8)). Extreme values of LW_{net}

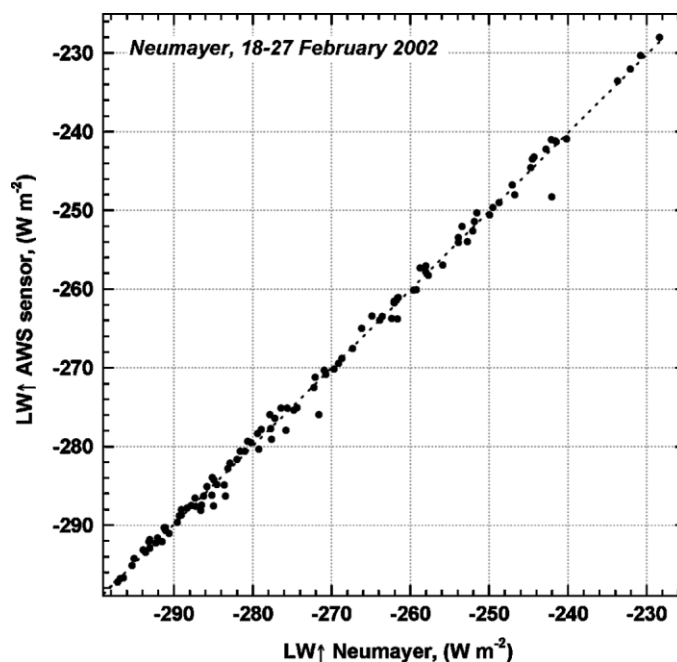


Figure 4. Comparison of 2 h average upwelling longwave radiation as measured with an AWS sensor (Kipp and Zonen CG3) and at Neumayer with a ventilated Eppley PIR, February 2002

found in Antarctica are 0 W m^{-2} under overcast conditions and -90 W m^{-2} under clear sky, summertime conditions around noon in the katabatic wind zone. A positive bias of 0.02 in ε thus introduces a maximum underestimation of T_s of about 0.5 K for typical Antarctic temperatures. However, this is an extreme value, and more typical values are 0.1–0.3 K. Because the value of ε is not known with any certainty, we choose to accept this additional uncertainty in T_s .

3. RESULTS

3.1. Validation of calculated sensible heat flux

Summertime eddy correlation measurements performed at the sites of AWS 6 (Bintanja, 2000) and AWS 9 (van As *et al.*, 2005a) allow us to assess the accuracy of calculated SHF values (Figure 5). Calculated and measured SHF agree well, with average differences less than 2 W m^{-2} and RMSDs of 4 W m^{-2} at AWS 6 (Svea Cross) and 3 W m^{-2} near AWS 9 (Kohnen base). Note that the sign change of SHF is well captured, which supports the absolute accuracy of the temperature gradient measurements at the AWS and the applicability of similarity theory.

3.2. Radiation, wind and temperature climate

First, we discuss some basic climate variables that influence SHF. Table II shows annual means and Figure 6 the seasonal cycle, based on monthly means, of net radiation R_{net} , 10 m wind speed $V_{10\text{m}}$ and temperature T for the period 1998–2001. To correct for elevation and continentality differences, temperature curves of AWSs 5, 6 and 9 in Figure 6(b) have been shifted upward by 1.2 K, 5.1 K and 21.1 K respectively. By doing so, we have assumed that the lapse rate along the surface during summer (when there is no or only a weak surface temperature inversion) is representative for the free atmospheric lapse rate during the entire year.

Van den Broeke *et al.* (2002) show that the katabatic pressure gradient force peaks in the winter in response to negative R_{net} (Figure 6(a)). The large-scale pressure gradient force, which in Antarctica generally acts in

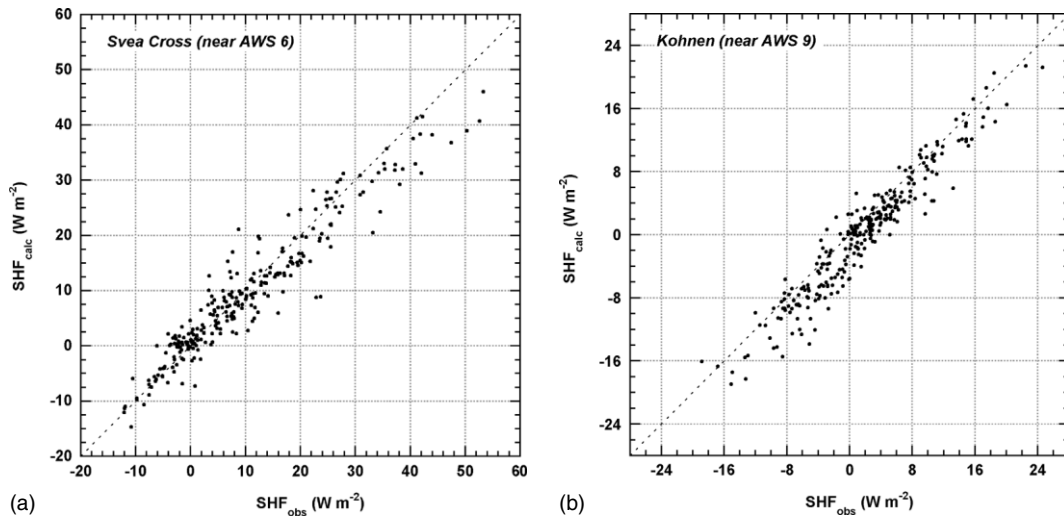


Figure 5. Comparison of calculated (using the bulk aerodynamic method) and measured (using eddy correlation data) SHF at (a) Svea Cross (January–February 1998) and (b) Kohnen base (January–February 2002)

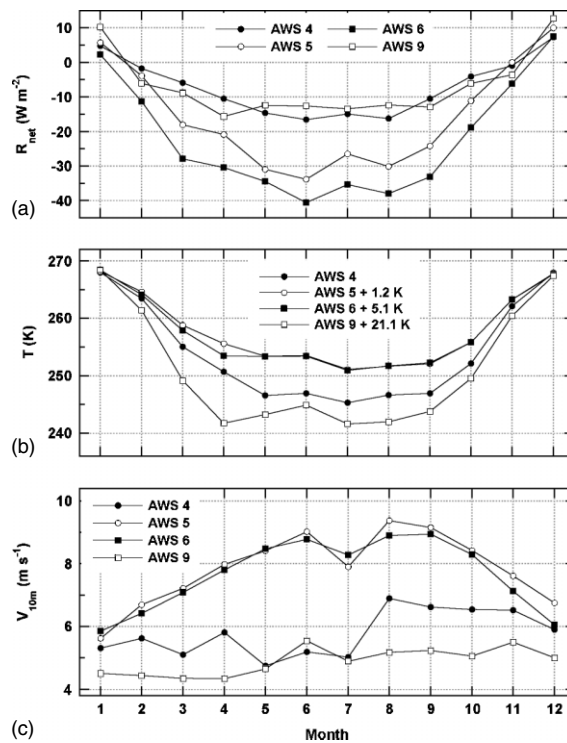


Figure 6. Average seasonal cycle (1998–2001) of (a) net radiation R_{net} , (b) AWS temperature and (c) 10 m wind speed. The temperature data have been corrected for elevation differences, assuming the summer lapse rate to be valid for the entire year

the same direction, i.e. down the slope, has rather constant magnitude through the year. As a result, AWSs 5 and 6 experience a pronounced seasonal cycle in wind speed (Figure 6(c)), in contrast to AWSs 4 and 9. The katabatic winds vertically mix the air, which results in 5–10 K higher near-surface temperatures (Figure 6(b)). This explains why katabatic wind regions are visible as ‘warm ‘signatures’ on satellite infrared

imagery (Bromwich, 1989; King *et al.*, 1998) and have elevated annual mean surface potential temperatures (van den Broeke *et al.*, 1999). This process is not active at AWSs 4 and 9, where temperatures decrease in winter until an approximate balance is struck between LW_{net} and G . Because snow conducts heat poorly, G is small, resulting in very low T_s . This process is especially effective on the plateau, where $LW \downarrow$ is small; the lowest temperature at AWS 9 measured at sensor height is -71.2°C .

In summer, katabatic forcing becomes weak and wind speeds are similar at all AWSs. They are still somewhat elevated in the katabatic wind zone because of night-time katabatic jets. The build-up of a strong surface-based temperature inversion in winter and its removal in summer forces a large seasonal temperature cycle of 23 K at AWS 4 and 27 K at AWS 9, compared with 17 K at AWSs 5 and 6.

3.3. Turbulent temperature scale

The turbulent temperature scale θ_* is a measure of the near-surface vertical temperature gradient, corrected for static stability effects. Figure 7 shows daily average values for the period 1998–2001, Figure 10(a) shows the average seasonal cycle based on monthly means. Unfortunately, wintertime riming of the radiation sensor windows occurs regularly at AWSs 4 and 9 (van den Broeke *et al.*, 2004b). Because the thermopile-type radiation sensor measures the temperature difference between the sensor surface and the object it looks at, both signals become zero during riming episodes, and so does the apparent temperature difference between the AWS sensor arm and the snow surface. This results in persistent near-zero wintertime values of θ_* (grey lines in Figure 7(a) and (d)). During these riming episodes, we reject T_s deduced from $LW \uparrow$ and solve the full energy balance equation for T_s in order to obtain values for θ_* and SHF. For $LW \downarrow$ we use parameterized values based on AWS temperature, as described in van den Broeke *et al.*, (2004b). This method produces realistic values of θ_* (black lines in Figure 7(a) and (d)).

The Antarctic SL is, on average, stably stratified, with θ_* having positive annual mean values ranging from 0.04 K at AWS 4 to 0.07–0.08 K at AWSs 5, 6 and 9 (Table II). Interdiurnal variability of θ_* is large at all sites (Figure 7). Maximum daily mean values of typically 0.2 K are found in winter. The seasonal cycle of θ_* shows a flat wintertime maximum at AWS 9 and a more peaked winter maximum at the other AWSs (Figure 10(a)), similar to what was found for the seasonal cycle of net radiation and temperature (Figure 6). Near-zero and negative θ_* values are found mainly in summer, when significant absorption of shortwave radiation in the daytime raises T_s above the air temperature. Convection also sporadically occurs in winter at AWSs 4 and 9 (Figure 7), when cold air is advected over a snow surface that is still relatively warm after a warm air intrusion. However, monthly means of θ_* are positive year-round at all AWSs (Figure 10(a)).

3.4. Friction velocity

Table II presents annual averages, Figure 8 daily averages and Figure 10(b) the seasonal cycle of friction velocity u_* , based on monthly means. Friction velocity is a measure of near-surface wind shear corrected for stability effects, and determines to a large extent the generation of turbulence in the stably stratified SL. Spatial variability in u_* results from variability in wind climate, $z_{0,v}$ and stability effects. The combined effect of these three factors is that annual mean u_* is smallest on the plateau (AWS 9) and almost two times larger in the katabatic wind zone (AWSs 5 and 6), and intermediate values are found on the coastal ice shelf (AWS 4) (Table II). Numerous short-lived peaks in u_* (Figure 8) result from high wind speed events when cyclones pass along the coast. As a result, these peaks are higher and more frequent at the coastal stations AWSs 4 and 5. Greatest absolute values of u_* are found in winter at AWS 5, where the combined effect of large-scale and katabatic forcing results in the strongest near-surface winds (Figure 6(c)). Frequency and amplitude of the peaks decrease towards the interior, where large-scale and katabatic forcing become less important (van den Broeke *et al.*, 2002).

At AWSs 5 and 6, peaks in u_* are superimposed on a seasonal cycle with a clear maximum in winter. Calms do not occur at these AWSs, as this would require the katabatic and large-scale pressure gradient forces to balance exactly; this is not likely to occur, because both pressure gradient forces generally act in the downslope direction. As a result, daily mean u_* values of 0.15–0.35 m s^{-1} are sustained throughout the winter (Figure 8). Remarkably, calms do not occur frequently at AWSs 4 and 9 either. This suggests

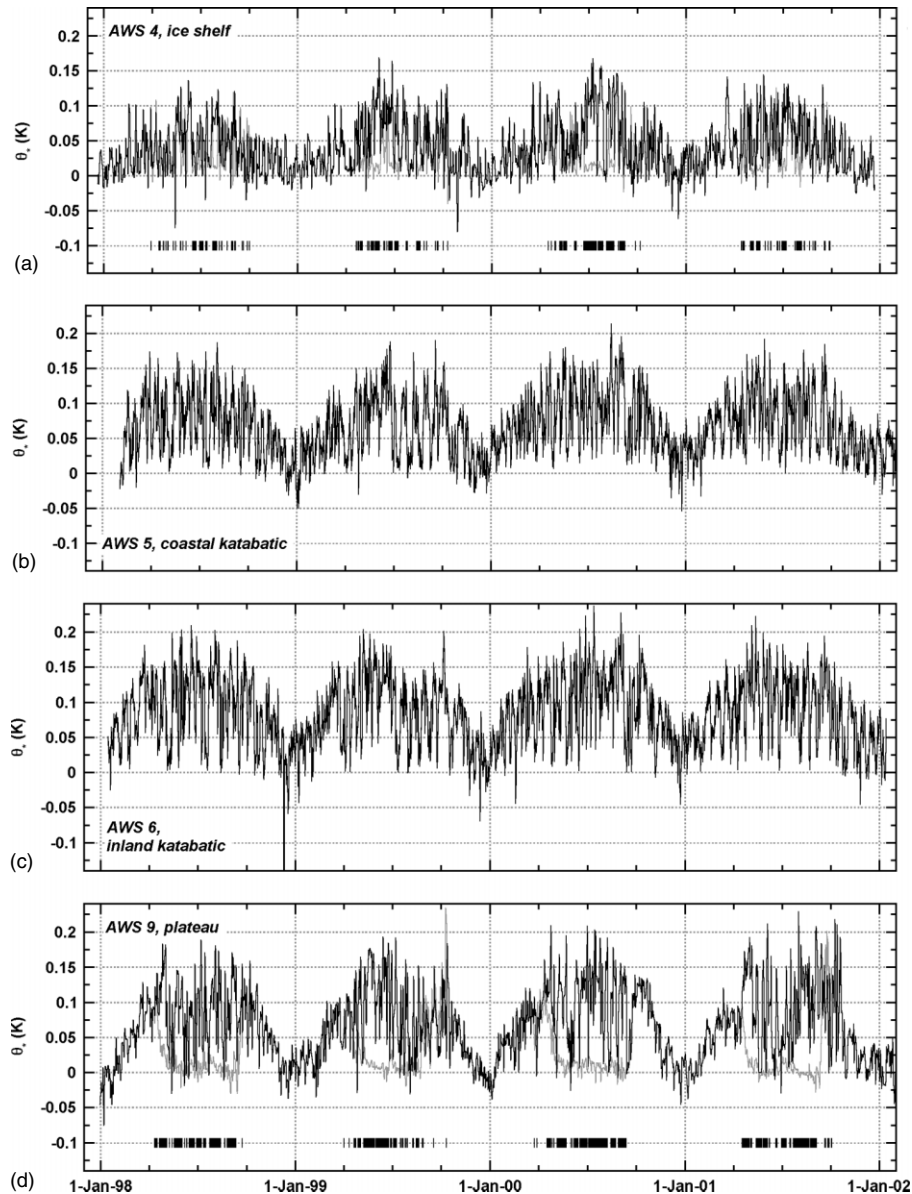


Figure 7. Daily means of turbulent temperature scale θ_* (1998–2001) at (a) AWS 4, (b) AWS 5, (c) AWS 6, and (d) AWS 9. The grey lines in (a) and (d) are original values that have not been corrected for riming of the longwave radiation sensor

that katabatic forcing could also be active at these sites. At AWS 9 this is supported by the formation of a katabatic jet during summer nights (van As *et al.*, 2005b). Although the surface slope on ice shelves is small, Heinemann (1988) and King (1989) have argued that katabatic forcing is also active on Antarctic ice shelves. Barrier wind activity may offer another explanation for persistent winds over the flat ice shelves bordering steep topography (Schwerdtfeger, 1975).

3.5. Kinematic and sensible heat fluxes

Table II shows annual means, Figure 9 daily averages and Figure 10 the seasonal cycle of SHF based on monthly means. To eliminate the effect of air density, which decreases by 30% from AWS 4 to AWS 9

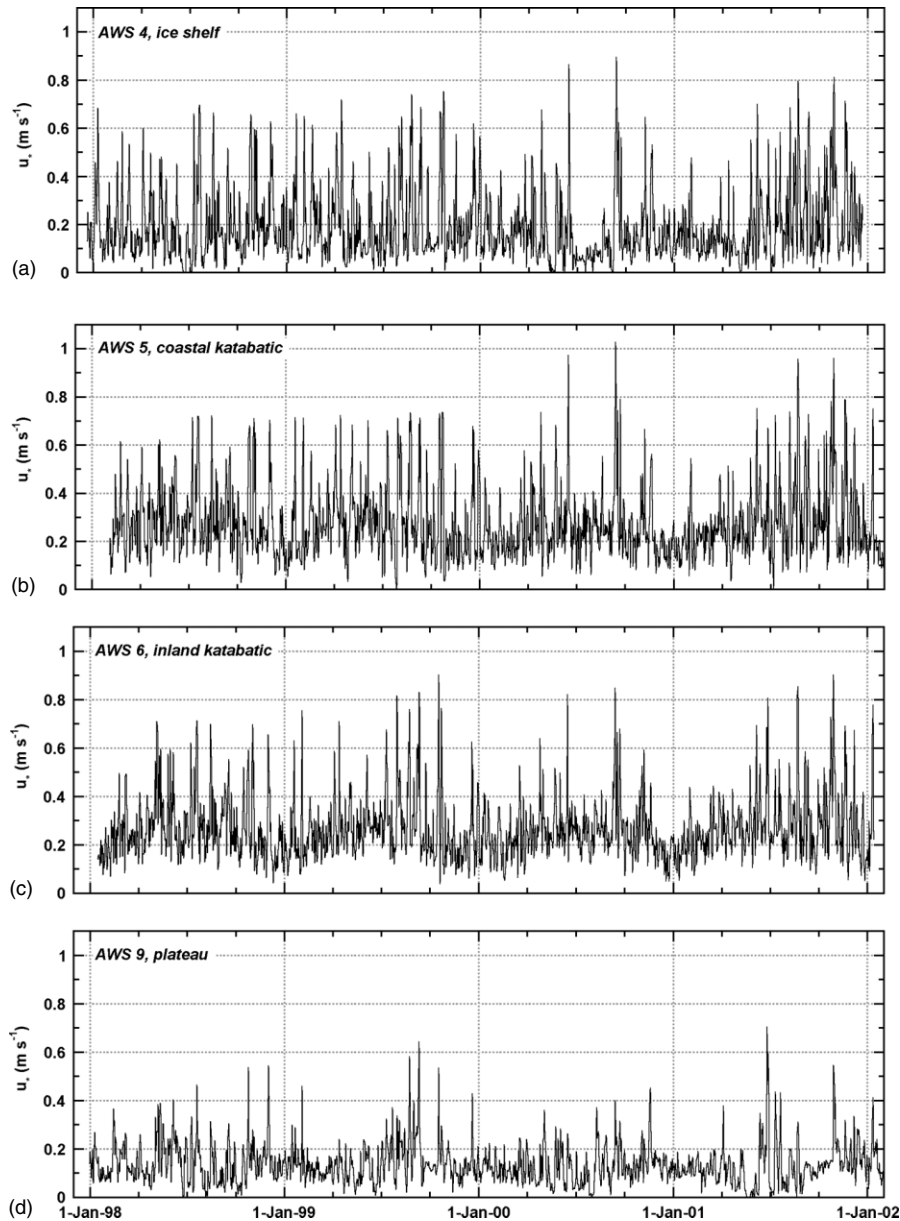


Figure 8. Daily means of turbulent velocity scale u_* (1998–2001) at (a) AWS 4, (b) AWS 5, (c) AWS 6, and (d) AWS 9

(Table II), we also included the kinematic heat flux $\text{KHF} = u_*\theta_*$ in Table II and Figure 10. Annual mean KHF in the katabatic wind zone is 2.5–3.5 times greater than on the ice shelf and on the plateau (Table II). In first order, these differences can be explained in terms of relative differences in annual mean θ_* and u_* ; at AWS 4 (ice shelf) u_* is large and θ_* is small, whereas on the plateau (AWS 9) u_* is small and θ_* is large. At AWSs 5 and 6, both are relatively large. However, there is also an important second-order effect: the ratio $\text{KHF}/u_*\theta_*$ (Table II) is largest in the katabatic wind zone, suggesting a higher degree of correlation of u_* and θ_* at these sites (see Section 4).

Interdiurnal variability in SHF is considerable at all AWS sites (Figure 9). During winter, daily mean SHF varies typically between 0 and 40 W m^{-2} at AWSs 4 and 9, whereas at AWSs 5 and 6 values of $10\text{--}70 \text{ W m}^{-2}$ are attained. Summertime daily means may be negative, but nowhere are they less than

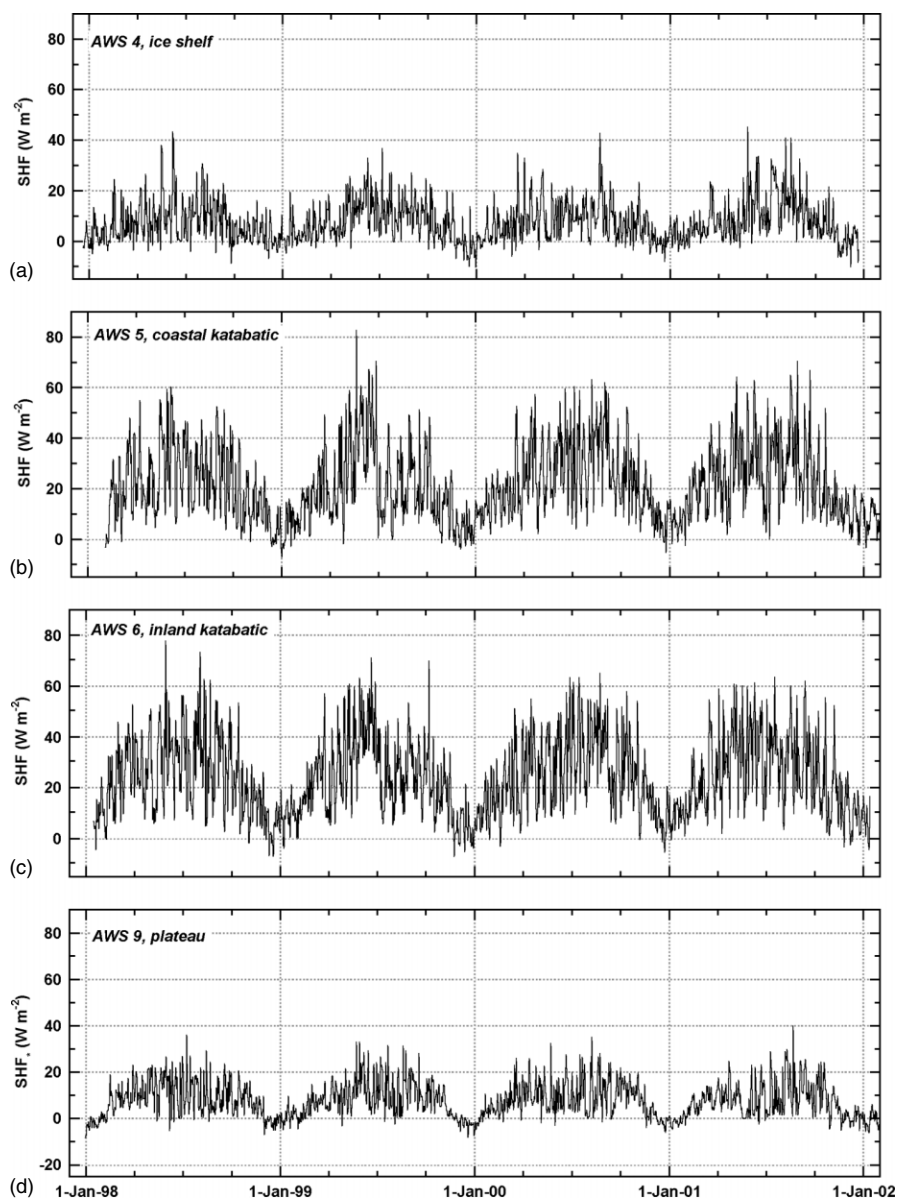


Figure 9. Daily mean values of calculated sensible heat flux SHF (1998–2001) at (a) AWS 4, (b) AWS 5, (c) AWS 6, and (d) AWS 9

-10 W m^{-2} . A seasonal cycle is present in the monthly means of all sites (Figure 10), with an amplitude of 10 W m^{-2} at AWSs 4 and 9 and typically 20 W m^{-2} in the katabatic wind zone. In December and January, SHF in the katabatic wind zone remains significantly positive, whereas at AWSs 4 and 9 it is close to zero.

4. DISCUSSION

4.1. The role of net radiation

Figure 11 shows that R_{net} determines the magnitude of the near-surface vertical temperature gradient, and hence SHF. During clear sky conditions in summer (December and January), mean daily R_{net} can become

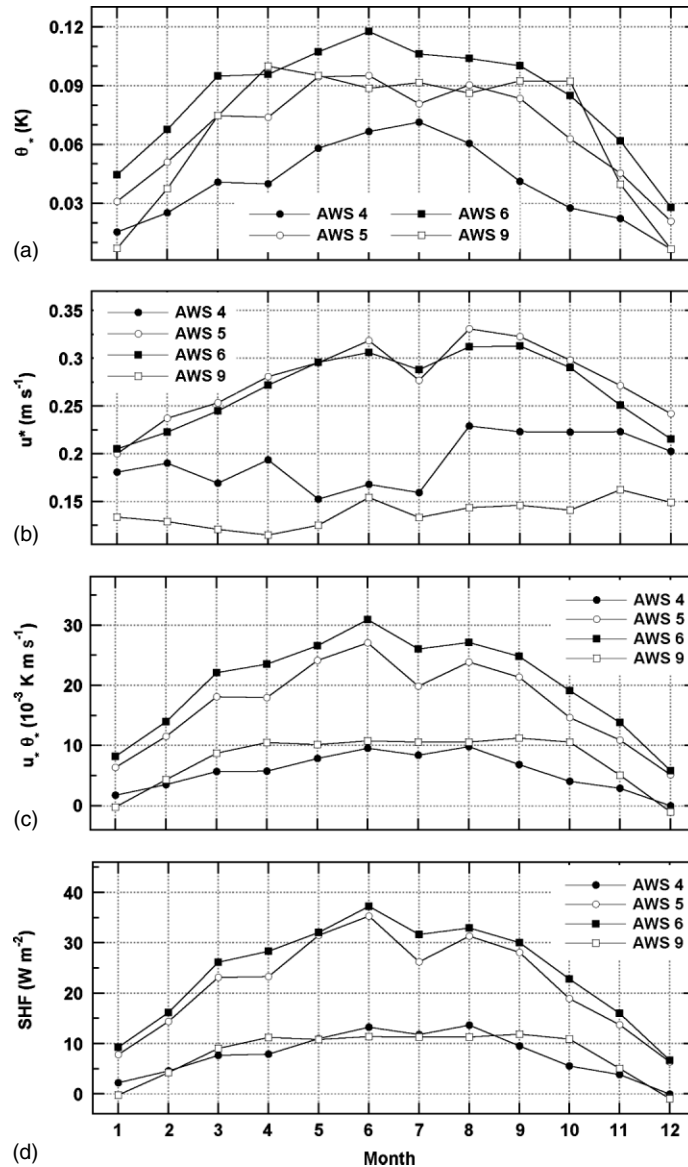


Figure 10. Average seasonal cycle (1998–2001), based on monthly means, of (a) turbulent temperature scale θ_* , (b) turbulent velocity scale u_* , (c) KHF and (d) SHF

significantly positive under the influence of shortwave radiation absorption (Figure 6(a)). When this happens, daily mean θ_* becomes small or negative, signifying weak convection. If daily mean $R_{\text{net}} = 0$, which represents overcast conditions and anomalously high surface temperatures both in winter and summer, θ_* is generally still positive (Figure 11). This implies a nonzero SHF, which is balanced by a G that becomes significantly negative when T_s is anomalously high. Although sublimation is another significant heat sink in summer, it is normally small during overcast conditions.

During winter, R_{net} (LW_{net}) is negative, resulting in positive values of θ_* at all sites (Figure 11). At the coastal site of AWS 4, frequent and thick clouds limit radiation loss, and hence θ_* and SHF. At AWS 9, predominantly clear skies enable large values of θ_* , but a lack of wind causes a strong static stability, which limits SHF at this site. At AWSs 5 and 6, clear skies enable large θ_* and strong winds enhance u_* , which limit stability effects (see next section).

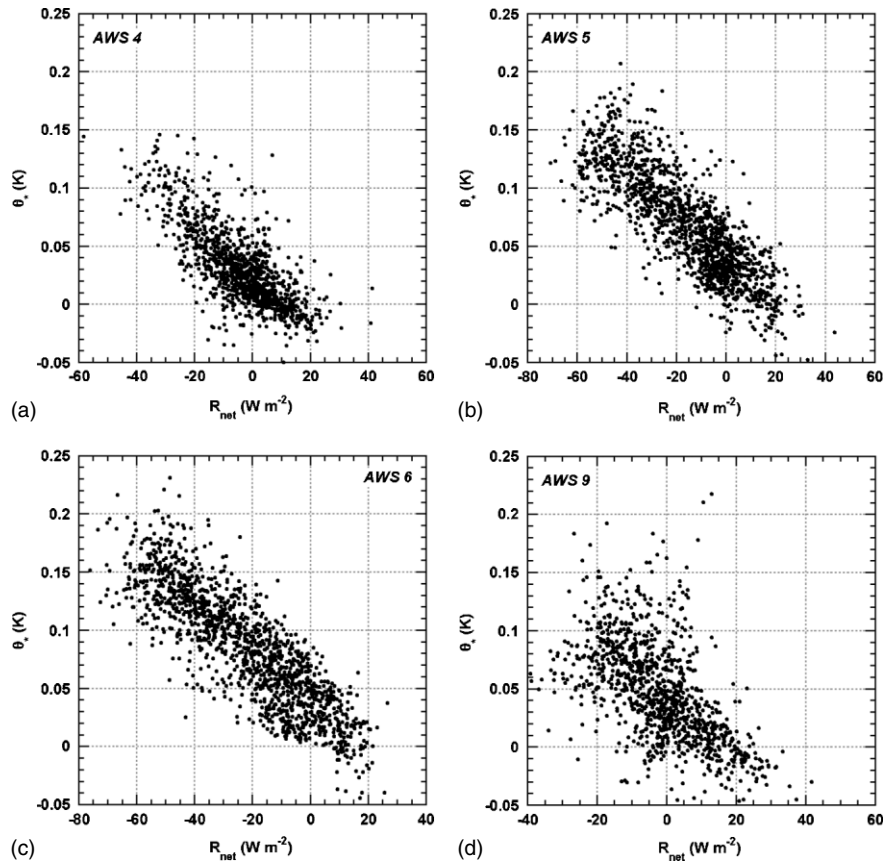


Figure 11. Daily means of turbulent temperature scale θ_* as a function of net radiation R_{net} , at all four AWSs (1998–2001)

4.2. The role of the stability correction

In the stably stratified SL, wind shear u_* must overcome the effect of buoyant destruction of turbulence. The stability corrections become important if Ψ_m and Ψ_h are similar in magnitude to $\ln(z_V/z_{0,V})$ and $\ln(z_T/z_{0,T})$, which happens during episodes of small u_* and large θ_* . On the other hand, strong winds and large u_* do not necessarily imply a large SHF. For instance, u_* spikes in Figure 8 are normally associated with depression activity and overcast conditions, during which near-neutral conditions prevail ($\theta_* \approx 0$).

In this section we quantify the role of stability effects on SHF. We do so by calculating SHF without taking into account the stability correction (SHF ($\Psi_m = \Psi_h = 0$) in Table II) and comparing it with the stability-corrected SHF. If we neglect the stability correction, SHF increases by 1.7 W m^{-2} (AWS 4) to 3.6 W m^{-2} (AWS 6). The relative increase is largest at AWS 9 (+33%). Figure 12 shows a histogram of the stability factor, defined as the ratio $\text{SHF}/\text{SHF}(\Psi_m = \Psi_h = 0)$, based on 2 h means. For all AWS sites, a stability correction of less than 10% occurs most frequently (stability factor between 0.9 and 1). Values smaller than 0.5 only regularly occur at AWSs 4 and 9.

To highlight the link between stability effects and local climate, Figures 13 and 14 present contours of θ_* and SHF as a function of AWS wind speed and the vertical temperature difference between surface and AWS sensor height. For simplicity we have assumed constant air density and sensor height (2 m for temperature and 2.5 m for wind speed). The dashed contours represent $\Psi_m = \Psi_h = 0$. Where dashed and solid lines deviate significantly, stability effects are important. We included daily mean observations for July (black dots) and January (white dots). We do not show AWS 5 results, because they are similar to AWS 6, nor do we show similar plots for u_* , because near-surface wind speed differences are usually larger than temperature differences, so that stability effects influence θ_* much more strongly than u_* .

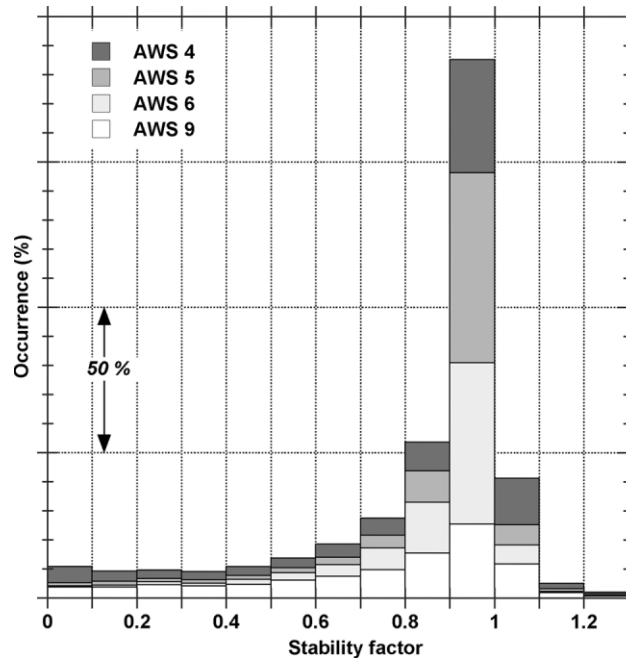


Figure 12. Stability factor histogram based on 2 h averages (1998–2001) for all four AWSs. Each y-axis marker represents 10%. For definition of stability factor, see text

At large temperature gradients and small wind speeds, θ_* (Figure 13) and SHF (Figure 14) become independent of the temperature difference; this is the very stable regime in which the effect on SHF of an increased temperature gradient in Equation (3) is entirely offset by an increase in Ψ_h so that θ_* remains constant. At AWSs 4 and 9, this regime occurs regularly during winter (black dots), so that SHF generally remains smaller than 20 W m^{-2} . The situation is very different at AWS 5 (not shown) and AWS 6: a positive correlation between wind speed and temperature gradient, caused by katabatic forcing, is clearly visible in the wintertime observations. This keeps the wintertime data out of the very stable regime and enables daily mean SHF of up to 60 W m^{-2} . Note that the largest values of SHF are found at intermediate wind speeds (6 to 8 m s^{-1} at 2.5 m) and large values of θ_* , which represents the purely katabatic regime. In January (white dots), temperature gradients, and hence θ_* and SHF, are generally small at all AWSs and stability effects unimportant.

4.3. Flow regimes

Other important parameters that determine the magnitude of SHF are the roughness lengths for momentum $z_{0,V}$ and temperature $z_{0,T}$. Together with wind velocity, $z_{0,V}$ determines the magnitude of $z_{0,T}$ (see Equation (6)), which explains the variation of θ_* with wind speed in the absence of stability corrections (dashed lines in Figure 13). A remarkable finding is that $z_{0,V}$ over the apparently homogeneous dry snow surface of Antarctica differs by an order of magnitude between the plateau and the katabatic wind zone (Figure 3). This difference may be caused by small sastrugi and/or sublimation-related surface roughness elements in the katabatic wind zone, which are absent in the low-wind speed and sublimation-free environment of the plateau. Future year-round eddy correlation measurements must indicate whether these differences in $z_{0,V}$ persist through the winter and from year to year.

The differences in contour lines in Figures 13 and 14 among the AWS result from differences in $z_{0,V}$ and the resulting different coupling of $z_{0,T}$ to u_* . If stability effects are taken into account (solid contours), then a local maximum in θ_* occurs at moderate wind speeds; at lower wind speeds, the stability correction suppresses θ_* , whereas at higher wind speeds the decrease of $z_{0,T}$ decreases θ_* . Note that the July observations at AWS 6

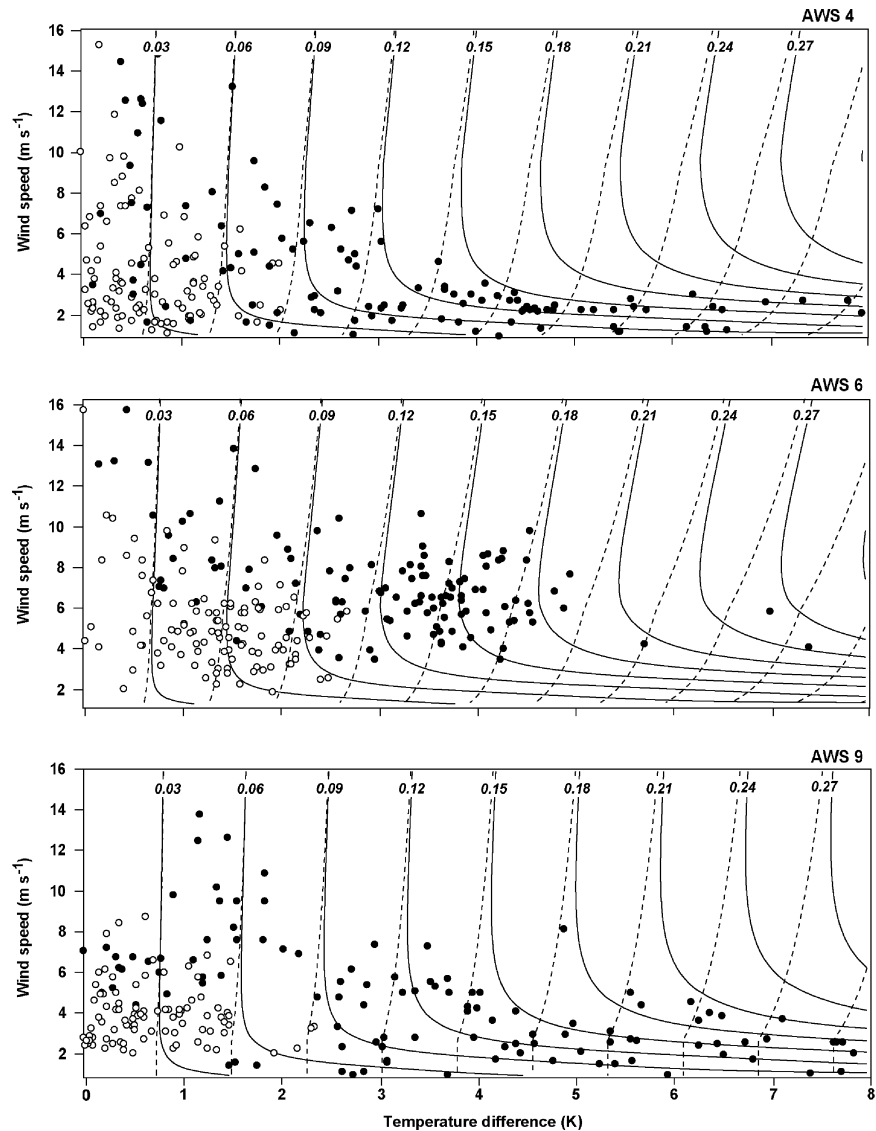


Figure 13. Contours of turbulent temperature scale θ_* calculated using the bulk aerodynamic method as a function of the 2 m-to-surface temperature difference (x -axis) and wind speed at 2.5 m (y -axis) for (a) AWS 4, (b) AWS 6 and (c) AWS 9. Dashed lines represent the case where stability correction has been neglected. Also included are observed daily means for July (black dots) and January (white dots)

tend to follow this optimum value. This maximum in θ_* can barely be detected at AWS 9, where the surface is aerodynamically smooth for most of the time and the dependence of $z_{0,T}$ on u_* consequently weaker.

Figure 15 shows the cumulative frequency of surface flow regimes. A low value of $z_{0,V}$ in combination with relatively weak winds leads to a surface that is aerodynamically smooth ($Re_* < 0.135$) for about 30% of the time at AWS 9. The remainder of the time the flow is in the transitional regime ($0.135 < Re_* < 2.5$). At AWS 4, 3% of the time the flow is in the aerodynamically smooth regime, 85% in the transitional regime and 12% in the rough regime. For AWSs 5 and 6 the surface is aerodynamically rough for 50% of the time; the remainder of the time the flow is in the transitional regime. The low Re_* flow at AWSs 4 and 9 leads to average values of $z_{0,T}$ that exceed $z_{0,V}$ (Table II). In the smooth regime, the value of $z_{0,T}$ no longer depends on flow characteristics, but assumes a constant value about 3.5 times the value of $z_{0,V}$ (i.e. 0.07 mm for AWS 9).

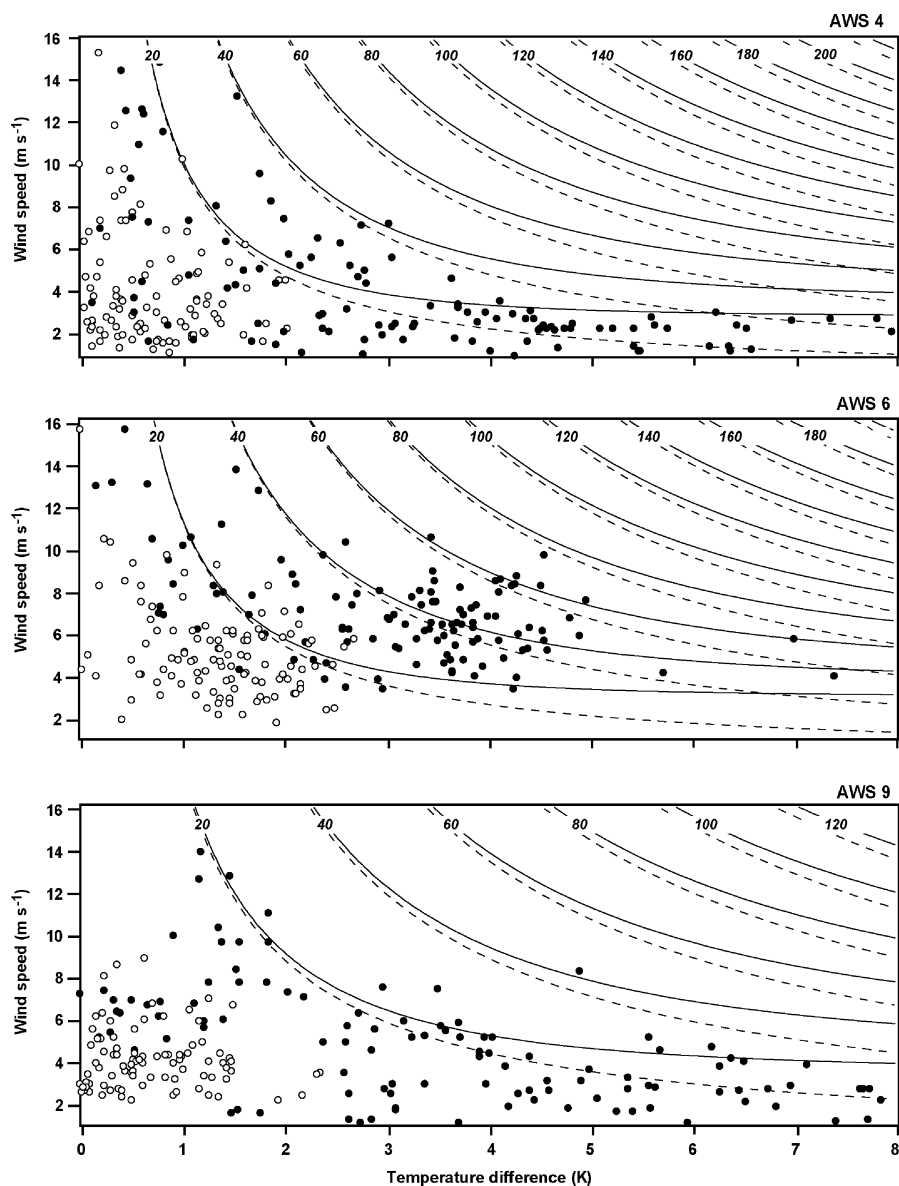


Figure 14. As Figure 13, but for SHF

5. SUMMARY AND CONCLUSIONS

We used data of four AWSs in DML, East Antarctica, to study the temporal and spatial variability of turbulent sensible heat exchange at the Antarctic snow surface. The SHF is determined using the aerodynamic ‘bulk’ method between a single AWS sensor level and the surface. The surface temperature is derived from measured upwelling longwave radiation and the surface roughness for momentum is determined using eddy correlation measurements at two AWS sites. Summertime eddy correlation measurements show that the surface roughness for momentum differs by almost an order of magnitude between the interior plateau (0.02 mm) and the katabatic wind zone (0.16 mm). We apply the equations presented by Andreas (1987) to calculate the roughness length for heat. A good agreement was found between calculated and directly measured SHF.

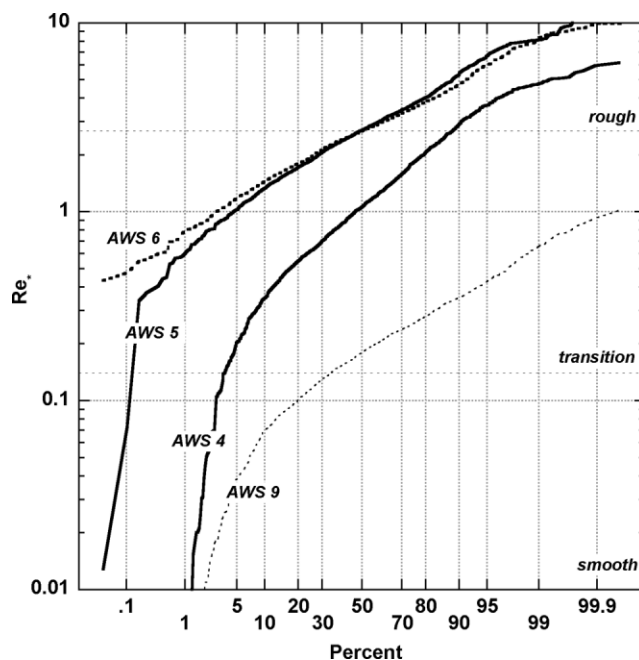


Figure 15. Cumulative frequency of roughness Reynolds number Re_* , based on 2 h averages (1998–2001). Also shown are the surface flow regimes according to Andreas (1987)

At all sites, the surface layer is, on average, stably stratified, so that annual mean SHF is positive. Annual mean SHF is similar for the coastal ice shelf and the interior plateau, i.e. 8 W m^{-2} . On the flat coastal ice shelf, frequent clouds limit surface radiation loss, and hence the vertical temperature gradient, resulting in a small average SHF. In contrast, clear sky conditions and strong temperature gradients prevail on the interior plateau. Here, the relatively weak winds, the aerodynamically smooth surface and stability effects limit the average value of SHF. The most favourable conditions for sensible heat exchange are found in the katabatic wind zone, where strong winds, in combination with clear skies and a relatively rough surface, result in annual mean SHF values of 22 to 24 W m^{-2} .

ACKNOWLEDGEMENTS

We thank the technical department of IMAU for designing, building and coordinating the maintenance of the AWS. Field parties of IMAU are thanked for maintenance work on AWSs 4, 5 and 6 and personnel of the Alfred Wegener Institut for the setting up and maintenance of AWS 9. Participants of SWEDARP are thanked for setting up and maintaining AWSs 4, 5 and 6. We gratefully acknowledge the use of Neumayer longwave radiation data. This work is partly funded by the Netherlands Antarctic Program (NAAP) and the Netherlands Organisation of Scientific Research, section Earth and Life Sciences (NWO/ALW). This work is a contribution to the 'European Project for Ice Coring in Antarctica' (EPICA), a joint ESF (European Science Foundation)/EC scientific programme, funded by the European Commission and by national contributions from Belgium, Denmark, France, Germany, Italy, the Netherlands, Norway, Sweden, Switzerland and the UK. This is EPICA publication no. 120.

REFERENCES

- Anderson PS. 1994. A method for rescaling humidity sensors at temperatures well below freezing. *Journal of Atmospheric and Oceanic Technology* **11**: 1388–1391.
 Allison I, Wendler G, Radok U. 1993. Climatology of the East Antarctic ice sheet (100°E to 140°E) derived from automatic weather stations. *Journal of Geophysical Research* **98**(D5): 8815–8823.

- Andreas EL. 1987. A theory for the scalar roughness and the scalar transfer coefficients over snow and sea ice. *Boundary-Layer Meteorology* **38**: 159–184.
- Andreas EL. 2002. Parameterizing scalar transfer over snow and ice: a review. *Journal of Hydrometeorology* **3**: 417–432.
- Bintanja R. 2000. Surface heat budget of Antarctic snow and blue ice: interpretation of spatial and temporal variability. *Journal of Geophysical Research* **105**: 24 387–24 407.
- Bintanja R. 2001. Modification of the wind speed profile caused by snowdrift: results from observations. *Quarterly Journal of the Royal Meteorological Society* **127**: 2417–2434.
- Bintanja R, van den Broeke MR. 1995. The surface energy balance of Antarctic snow and blue ice. *Journal of Applied Meteorology* **34**: 902–926.
- Bintanja R, Jonsson S, Knap WH. 1997. The annual cycle of the surface energy balance of Antarctic blue ice. *Journal of Geophysical Research* **102**(D2): 1867–1881.
- Bromwich DH. 1989. Satellite analyses of Antarctic katabatic wind behavior. *Bulletin of the American Meteorological Society* **70**: 738–749.
- Caroll JJ. 1982. Long-term means and short-term variability of the surface energy balance components at the South Pole. *Journal of Geophysical Research* **87**(C6): 4277–4286.
- Clow GD, McKay CP, Simmons Jr GM, Wharton Jr RA. 1988. Climatological observations and predicted sublimation rates at Lake Hoare, Antarctica. *Journal of Climate* **1**: 715–728.
- Déry SJ, Yau MK. 2002. Large-scale mass balance effects of blowing snow and surface sublimation. *Journal of Geophysical Research* **107**: 4679. DOI: 10.1029/2001JD001251.
- Déry SJ, Taylor PA, Xiao J. 1998. The thermodynamic effects of sublimating, blowing snow in the atmospheric boundary layer. *Boundary-Layer Meteorology* **89**: 251–283.
- Dyer AJ. 1974. A review of flux–profile relationships. *Boundary-Layer Meteorology* **7**: 363–372.
- Gallée H, Guyomarch G, Brun E. 2001. Impact of snow drift on the Antarctic ice sheet surface mass balance: possible sensitivity to snow surface properties. *Boundary-Layer Meteorology* **99**: 1–19.
- Heinemann G. 1988. Structure and energy budget of the boundary layer in the vicinity of the Filchner Ronne ice shelf front (Antarctica). *Beiträge zur Physik der Atmosphäre* **61**(3): 244–258.
- Heinemann G, Rose L. 1990. Surface energy balance, parametrizations of boundary-layer heights and the application of resistance laws near an Antarctic ice shelf front. *Boundary-Layer Meteorology* **51**: 123–158.
- Helsen MM, van de Wal RSW, van den Broeke MR, Kerstel ERTh, Masson-Delmotte V, Meijer HAJ, Reijmer CH, Scheele MP. In press. Modelling the isotopic composition of snow using backward trajectories: a particular precipitation event in Dronning Maud Land, Antarctica. *Annals of Glaciology*.
- Holtslag AAM, de Bruijn EIF. 1988. Applied modelling of the nighttime surface energy balance over land. *Journal of Applied Meteorology* **27**: 689–704.
- King JC. 1989. Low-level wind profiles at an Antarctic coastal station. *Antarctic Science* **1**(2): 169–178.
- King JC, Anderson PS. 1994. Heat and water vapour fluxes and scalar roughness over an Antarctic ice shelf. *Boundary-Layer Meteorology* **69**: 101–121.
- King JC, Turner J. 1997. *Antarctic Meteorology and Climatology*. Cambridge University Press.
- King JC, Anderson PS, Smith MC, Mobbs SD. 1996. The surface energy and mass balance at Halley, Antarctica during winter. *Journal of Geophysical Research* **101**(D14): 19 119–19 128.
- King JC, Varley MJ, Lachlan-Cope TA. 1998. Using satellite thermal infrared imagery to study boundary-layer structure in an Antarctic katabatic wind region. *International Journal of Remote Sensing* **19**: 3335–3348.
- Li L, Pomeroy JW. 1997. Estimates of threshold wind speeds for snow transport using meteorological data. *Journal of Applied Meteorology* **36**: 205–213.
- Liljequist GH. 1957. Energy exchange over an Antarctic snow field: surface inversion and turbulent exchange. *Norwegian, British, Swedish Antarctic Expedition, 1949–1952. Scientific Results*, Vol 2, Part 1d. Norsk Polarinstittutt: Oslo.
- Mann GW, Anderson PS, Mobbs SD. 2000. Profile measurements of blowing snow at Halley, Antarctica. *Journal of Geophysical Research* **105**: 24 491–24 508.
- Ohata T, Kobayashi S, Ishikawa N, Kawaguchi S. 1985. Heat balance at the snow surface in a katabatic wind zone, East Antarctica. *Annals of Glaciology* **6**: 174–177.
- Ohmura A, *et al.* 1998. Baseline Surface Radiation Network (BSRN/WRMC), a new precision radiometry for climate research. *Bulletin of the American Meteorological Society* **79**: 2115–2136.
- Reijmer CH, Oerlemans J. 2002. Temporal and spatial variability of the surface energy balance in Dronning Maud Land, East Antarctica. *Journal of Geophysical Research* **107**: 4759. DOI: 10.1029/2000JD000110.
- Reijmer CH, van den Broeke MR. 2003. Temporal and spatial variability of the surface mass balance in Dronning Maud Land, Antarctica, as derived from automatic weather stations. *Journal of Glaciology* **49**(167): 512–520.
- Renfrew IA, Anderson PS. 2002. The surface climatology of an ordinary katabatic wind regime in Coats Land, Antarctica. *Tellus, Series A: Dynamic Meteorology and Oceanography* **54**: 464–484.
- Schwerdtfeger W. 1975. The effect of the Antarctic peninsula on the temperature regime of the Weddell Sea. *Monthly Weather Review* **103**: 45–51.
- Stearns CR, Weidner GA. 1993. Sensible and latent heat flux estimates in Antarctica, In *Antarctic Meteorology and Climatology, Studies Based on Automatic Weather Stations*. Bromwich DH, Stearns CR (eds). *Antarctic Research Series*, vol. 61. Washington DC: 109–138.
- Van As D, van den Broeke MR, van de Wal RSW, Reijmer CH. 2005a. The summertime energy balance on the high Antarctic plateau. *Boundary-Layer Meteorology* **15**(2): 289–317.
- Van As D, van den Broeke MR, van de Wal RSW. 2005b. Daily cycle of the surface layer on the high Antarctic plateau. *Antarctic Science* **17**(1): 121–133.
- Van den Broeke MR, Winther J-G, Isaksson E, Pinglot JF, Karlöf L, Eiken T, Conrads L. 1999. Climate variables along a traverse line in Dronning Maud Land, East Antarctica. *Journal of Glaciology* **45**: 295–302.

- Van den Broeke MR, van Lipzig NPM, van Meijgaard E. 2002. Momentum budget of the East-Antarctic atmospheric boundary layer: results of a regional climate model. *Journal of the Atmospheric Sciences* **59**: 3117–3129.
- Van den Broeke MR, van As D, Reijmer CH, van de Wal RSW. 2004a. The surface radiation balance in Antarctica as measured with automatic weather stations. *Journal of Geophysical Research* **109**: D09103. DOI: 10.1029/2003JD004394.
- Van den Broeke MR, van As D, Reijmer CH, van de Wal RSW. 2004b. Assessing and improving the quality of unattended radiation observations in Antarctica. *Journal of Atmospheric and Oceanic Technology* **21**(9): 1417–1431.
- Van den Broeke MR, Reijmer CH, van de Wal RSW. In press a. A study of the Antarctic mass balance using automatic weather stations. *Journal of Glaciology*.
- Van den Broeke MR, Reijmer CH, van As D, van de Wal RSW, Oerlemans J. In press b. Seasonal cycles of Antarctic surface energy balance from automatic weather stations. *Annals of Glaciology*.
- Wamser C, Lykossov VN. 1995. On the friction velocity during blowing snow. *Beiträge zur Physik der Atmosphäre* **68**(1): 85–94.
- Wendler G, Ishikawa N, Kodama Y. 1988. The heat balance of the icy slope of Adélie Land, Eastern Antarctica. *Journal of Applied Meteorology* **27**: 52–65.
- Wiscombe WJ, Warren SG. 1980. A model for the spectral albedo of snow: I: pure snow. *Journal of the Atmospheric Science* **37**: 2712–2733.